EUROFUSION WPPMI-PR(16) 16114

M Siccinio et al.

# A 0D stationary model for the evaluation of the degree of detachment on the divertor plates

Preprint of Paper to be submitted for publication in
Plasma Physics and Controlled Fusion

This work has been carried out within the framework of the EUROfusion Consortium and has received funding from the Euratom research and training programme 2014-2018 under grant agreement No 633053. The views and opinions expressed herein do not necessarily reflect those of the European Commission.

# A 0D stationary model for the evaluation of the degree of detachment on the divertor plates

M. Siccinio[a*], E. Fable[a], K. Lackner[a], A. Scarabosio[a], R. P. Wenninger[a,b], H. Zohm[a]

[a] *Max Planck Institut für Plasmaphysik, Boltzmannstr. 2, 85748 Garching bei München, Germany*

[b] *EUROfusion Consortium, PPPT Department, Boltzmannstr. 2, 85748 Garching bei München, Germany*

**Abstract**

A 0D analytical stationary model to estimate the degree of detachment on the divertor plates is derived, starting from previous works of Igitkhanov [1, 2, 3]. It accounts for heat convection, conduction, flux expansion at the divertor plates, impurity radiation and contains a simplified balance for the neutrals. The upstream particle flux $\Gamma_{up}$ (or, alternatively, the density upstream $n_{up}$), the heat flux in the scrape-off layer (SOL) $q_{up}$ and the impurity concentrations are required as input, whereas the temperatures at the plate and at the separatrix are not fixed *a priori*. The routine has been mainly developed for system codes, or more in general for control studies in the framework of the preliminary design phase for the reactor DEMO, its simplicity being therefore justified by the purpose of keeping the calculation times as low as possible. A benchmark against a more detailed 1D routine [4] has been performed, finding a reasonable agreement. Furthermore, a coupling of the model with the 1.5D transport code ASTRA [5, 6] to illustrate its possible usages is also presented.

# 1 Introduction

The numerous criticalities associated to the feasibility of a future nuclear fusion power plant are strictly connected one to the other. Thus, a comprehensive approach to the design of the prototypical machine DEMO is necessary, especially in the currently ongoing pre-conceptual design analysis phase. From this point of view, the realisation of models which are at the same time simple but able to capture the most relevant aspects of the fusion plasma physics is of primary importance. The problem of power exhaust at the divertor plates is commonly acknowledged to be a crucial issue for the design of a future nuclear fusion reactor [7]. It has already been observed [8] that, in view of the high power crossing the separatrix (around 150 MW for a conventional DEMO 1 scenario with $P_{fus} \sim 2000$ MW [9]) and of the relatively small area on which it is supposed to be deposited (according to well-known Eich scaling [10, 11]), it would be impossible for DEMO to operate in a fully attached divertor regime without greatly exceeding the technological limit of 10-15 MW/m$^2$ of power exhaust

*Contact: mattia.siccinio@ipp.mpg.de

on the divertor plates. Thus, an at least partial detachment is mandatory to be achieved in order to reduce the incoming plasma flow, and, in parallel, it is very important to develop some predictive capability to identify the conditions under which the machine can be safely operated.

In this paper, a 0D model for the estimate of the divertor detachment degree for given upstream conditions is presented. The relatively simple 0D set of equations the model consists in make this tool particularly appropriate for being employed in system codes, or more in general for the search of optimised design points on a power plant level. In spite of its unavoidably simplistic approach, justified by the aim of keeping the computational time as low as possible in view of a coupling with more comprehensive design softwares, the model embraces the prominent physical mechanisms determining the onset of detachment (heat convection, heat conduction, flux expansion at the divertor plates, impurity radiation, ionisation and charge exchange), possessing therefore a high flexibility together with a reasonable degree of accuracy.

The paper is structured as follows: in section 2, the equations are derived and presented, in section 3 the validation of the model by means of a more detailed 1D routine (developed by Kallenbach *et al.* and in turn validated against experimental data of ASDEX Upgrade, see [4]) is discussed. Section 4 contains an exemplary employement of the tool, which has been coupled with with the 1.5D transport code ASTRA [5, 6] to investigate the efficiency of different impurity mixings, whereas conclusions are drawn in section 5.

# 2 The Model

The magnetic field line (*rectius*, the flux tube) of length $L_\parallel$ which connects the outer midplane to the divertor plate is artificially subdivided into two regions, labelled with I and II. More specifically:

- **Region I**. Therein, the heat is supposed to be transported along the field line only via *conduction*, whereas the static pressure is supposed to be constant. Impurity radiation is present, and the relative concentration of the radiative species is supposed to be spacially homogeneous. The region extends from the outer midplane for a distance indicated with $L_r$, which is an output of the model.
- **Region II**. This is the *convective* region, which starts from $L_r$ and reaches the target plate. It is characterised by pure convection (assuming Mach number $M = 1$), constant total pressure and impurity radiation, with the relative concentration of the radiative species again supposed to be homogeneous. Its length is denoted with $L_m = L_\parallel - L_r$. The transition between conduction and convection is supposed to take place where a critical temperature $T_C$, which is a free parameter in the model, is reached.

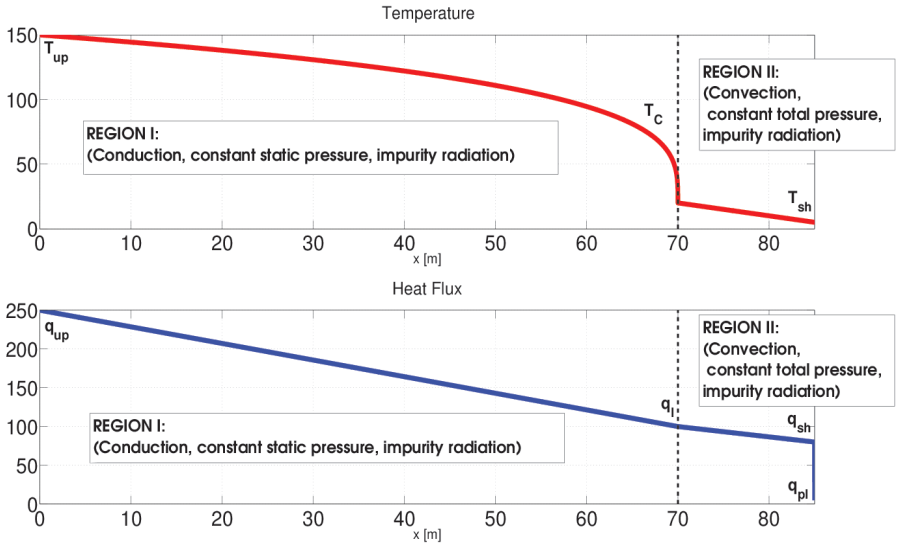


Figure 1: Schematic representation of the field line between outer midplane and target plate. The difference between $q_{sh}$ and $q_{pl}$ is due both to momentum losses, that reduce the particle flux, and to the purely geometrical effect of the inclination of the tiles with respect to the magnetic field line. Other variations of the flux tube cross section along the field line itself are not accounted for. The vertical dashed line has been set at $x = L_r$ to identify the boundary between the conductive and the convective region. The temperature and $q_{\|}$ profiles represented here are purely illustrative.

The temperature at the plates, indicated with $T_{sh}$, acts as input for the momentum loss calculation, discussed below. In order to keep the model simple enough, the interaction with the neutrals is assumed not to massively affect the heat transport and the temperature profiles, which are therefore calculated at constant total pressure. In the following, quantities defined at the outer midplane are denoted by the subscript *up* and quantities at the interface between the conductive and the convective region with the subscript $I$. A further distinction is introduced between quantities defined at the end of the magnetic fieldline *but without having considered momentum losses* , indicated with *sh*, and quantities actually reaching the target plate after the interaction with the neutrals, indicated with the subscript *pl*. Fig.1 schematically depicts the subdivision of the magnetic field line.

Analogously to the well-known two-point-model [12], it is here supposed that the entire particle and energy flux crossing the separatrix be concentrated at the outer midplane. In principle, region I could be understood as the “scrape-

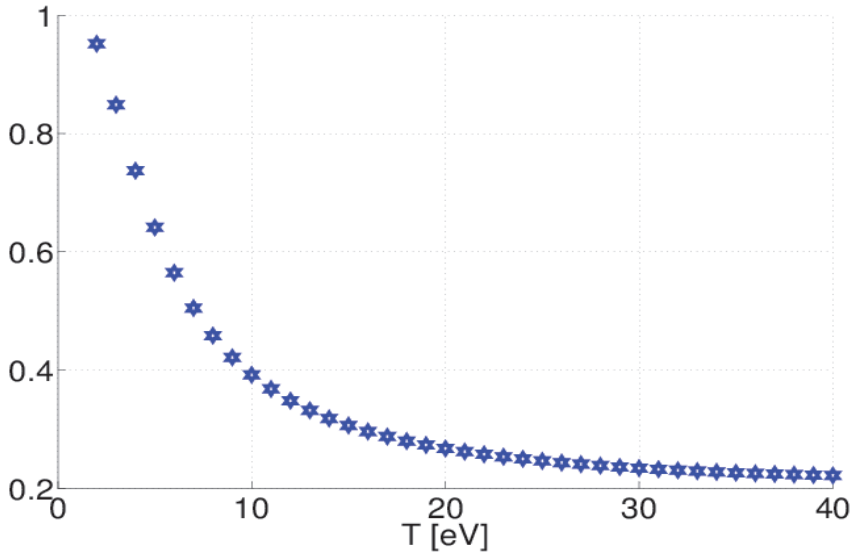


Figure 2: Momentum loss factor $f_m$ as a function of the temperature according to Eq.17.

off layer" region (hencefort SOL), whereas the conductive region represents the "divertor" region. *Such identification is however somehow misleading, because the transition between the two regions is not supposed to be located at a precise position along the field line, but it moves according to the temperature profile.* In particular, if the temperature remains above $T_C$ everywhere, $L_r$ coincides with $L_\parallel$ and no convective region is considered at all, although, obviously, the divertor is still present. In the following, a description of the equations in the model is given.

## 2.1 Density Upstream

The model has in input the particle flux at the separatrix. However, what enters the successive equations is rather the density at the same location, $n_{up}$. To connect the two quantities, a radial density profile which decays exponentially outside the separatrix at the outer midplane is assumed, namely

$$n(r) = n_{up} \exp\left(-\frac{r}{\lambda_p}\right) \tag{1}$$

(with $r = 0$ identifying the separatrix), together with a diffusive ansatz across the magnetic field lines

$$\Gamma_{up} = -D_r \left.\frac{\mathrm{d}n}{\mathrm{d}r}\right|_{r=0}. \tag{2}$$

Putting the two equations together, one finds

$$n_{up} = \lambda_p \frac{\Gamma_{up}}{D_r} \tag{3}$$

The value of the two parameters $\lambda_p$ and $D_r$ has to be prescribed by the user. Reasonable values are $\lambda_p = 5$ mm or more, $D_r = 1$ m$^2$/sec, or less. The use of Eq.3 could be avoided if the value of $n_{up}$ is known.

## 2.2 Region I

The equations for the conductive region are derived from two 1D equations plus one boundary condition, which are subsequently manipulated to obtain a set of 0D equations. The heat flux $q(x)$ ($x$ being the coordinate along the field line, $x = 0$ identifying the outer midplane and $x = L_\parallel$ corresponding to the target plate) is supposed to be transported purely via conduction, namely

$$q\left(x\right) = -\chi_0 T\left(x\right)^{5/2} \frac{\mathrm{d}T\left(x\right)}{\mathrm{d}x}, \tag{4}$$

with $T(x)$ the local temperature (we assume ion and electron temperatures to be everywhere equal) and $\chi_0 T^{5/2}$ representing the well-known Spitzer-Härm conductivity (with $\chi_0 = 2390$ W/m eV$^{7/2}$). Impurity radiation lets the heat flux vary along the field line,

$$\frac{\mathrm{d}q\left(x\right)}{\mathrm{d}x} = -n(x)^2 c_z^I l_z(T) \tag{5}$$

where $c_z^I$ is the (constant) fraction of impurities with respect to the electron density $n(x)$, while $l_z$ is the cooling factor. These equations can be combined and then integrated, leading to

$$q(T)^2 = q_I^2 + 2\chi_0 (n_{up} T_{up})^2 c_z^I \int_{T_C}^{T} \mathrm{d}T \sqrt{T} l_z(T), \tag{6}$$

having exploited the constancy of the static pressure, i.e. $n(x)T(x) = n_{up}T_{up}$. This equation, originally derived by Lengyel [13], for $T = T_{up}$ reads

$$q_{up}^2 = q_I^2 + 2\chi_0 (n_{up} T_{up})^2 c_z^I \int_{T_C}^{T_{up}} \mathrm{d}T \sqrt{T} l_z(T). \tag{7}$$

The second equation directly descends from of Eq.4. Observing that the heat flux depends on $x$ only through the temperature, it is possible to write

$$\mathrm{d}x = -\chi_0 T^{5/2} \frac{\mathrm{d}T}{q(T)}. \tag{8}$$

Integrating on the length of the conductive domain, one finds

$$L_r = \chi_0 \int_{T_C}^{T_{up}} \mathrm{d}T \frac{T^{5/2}}{q(T)}, \tag{9}$$

where $q(T)$ is known from Eq.6. The last equation corresponds to the purely conductive boundary condition at the interface between region I and II, assuming constant total pressure, Mach number $M = 1$ (these two conditions together leading to $n_{up}T_{up} = 2n_{sh}T_{sh}$) and having introduced the usual sheat multiplication factor $\gamma$,

$$q_I = \frac{\gamma}{2} e n_{up} T_{up} c_{s0} \sqrt{T_C}. \tag{10}$$

Here, $e$ indicates the electron charge, $m_i$ the ion mass, and $c_{s0} = \sqrt{2e/m_i}$ is the sound speed calculated at $T_{ref} = 1$ eV. The three unknowns are $q_I$, $T_{up}$ and $L_r$. If no convective region is present (i.e. no solution with $L_r < L_\parallel$ can be found), the transition temperature $T_C$ (known) is substituted by $T_{sh}$ (unknown), whereas $L_r$ (unknown) is set equal to $L_\parallel$ (known), leaving otherwise the equations unchanged.

## 2.3 Region II

In the convective region, the equation for $q_{sh}$ is derived on the same footing of Eq.3, accounting for the radiation losses - contrarily to what happened in the original Igitkhanov model [1, 2, 3], where divertor radiation was not considered. Starting point is the impurity radiation equation Eq.5, again assuming constant total pressure and $M = 1$,

$$\frac{\mathrm{d}q\,(x)}{\mathrm{d}x} = -\frac{n_{up}^2 T_{up}^2}{4} c_z^{II} \frac{l_z(T)}{T(x)^2} \tag{11}$$

together with the equation for the convected power (which in our assumptions coincides with the total power)

$$q(x) = \frac{\gamma}{2} e n_{up} T_{up} c_{s0} \sqrt{T(x)}. \tag{12}$$

Eq.12 can be derived with respect to $x$ and then substituted into Eq.11. Employing straightforward algebra, one finds

$$\int_{T_{sh}}^{T_C} \mathrm{d}T \frac{T^{3/2}}{l_z(T)} = \frac{n_{up} T_{up} c_z^{II}}{\gamma e c_{s0}} L_m \tag{13}$$

The model is closed by the boundary condition at the plate

$$q_{sh} = \frac{\gamma}{2} e n_{up} T_{up} c_{s0} \sqrt{T_{sh}}. \tag{14}$$

Eq. 13 and 14 are employed to determine the two unknowns $T_{sh}$ and $q_{sh}$. Note that in the limit of no radiative impurities we recover $T_{sh} = T_C$ and $q_{sh} = q_I$, which is consistent with the assumed pure convective heat transport.

## 2.4 Neutrals and Divertor Detachment

For the momentum loss due to the interaction of the neutrals with the incoming plasma flow, we employ a very simple model taken from the literature (originally developed by Self and Ewald [14], it has been included in the comprehensive review by Pitcher and Stangeby [15]). This model is based on the competition between charge exchange and ionisation, which mainly depends on the plasma temperature $T_{sh}$. It is herewith stressed that, in principle, *every* modellisation for the neutrals requiring in input only $T_{sh}$ can be implemented at this point, this providing our tool a certain degree of flexibility. Estimating $\varphi$ - the ratio between the ionisation and the charge exchange cross sections - with [16]

$$\varphi = 2.8 \frac{\exp\left(-13.6/T_{sh}\right) T_{sh}^{0.19}}{6 + 0.073 T_{sh}}, \tag{15}$$

one introduces the dimensionless parameter $\alpha_{ps}$

$$\alpha_{ps} = \frac{\varphi}{1+\varphi}. \tag{16}$$

The momentum loss factor $f_m$ - defined as the ratio between the total pressure losses and the total pressure upstream - is calculated as [14, 15]

$$f_m = 1 - 2\left(\frac{\alpha_{ps}}{1+\alpha_{ps}}\right)^{(\alpha_{ps}+1)/2}. \tag{17}$$

The corresponding thermal flux at the plates reads then

$$q_{pl} = (1-f_m)\frac{q_{sh}}{f_x} = (1-f_m)\frac{\gamma}{2f_x} e n_{up} T_{up} c_{s0} \sqrt{T_{sh}} \tag{18}$$

where $f_x$ is the geometrical factor which accounts for the inclination of the target plate with respect to the magnetic field line (other variations in the flux tube cross section along the field line are not accounted for). The momentum loss factor $f_m$ is employed in the model as the measure of the detachment degree. In particular, $f_m = 0$ corresponds to a fully attached situation, whereas $f_m = 1$ corresponds to a vanishing flux on the target plate. The usual definition of degree of detachment $\Gamma$, i.e. the ratio between the "ideal" flux calculated by means of the two-point model and the actual flux, is recovered as

$$\Gamma = \frac{1}{1-f_m}. \tag{19}$$

Fig.2 shows $f_m$ as a function of the temperature according to Eq.15-17.

## 2.5 Overview

The model consists in eight equations and eight unknowns ($n_{up}$, $T_{up}$, $q_I$, $L_r$, $T_{sh}$, $q_{sh}$, $f_m$, $q_{pl}$), which reduce to six in the purely conductive case (as $q_I = q_{sh}$

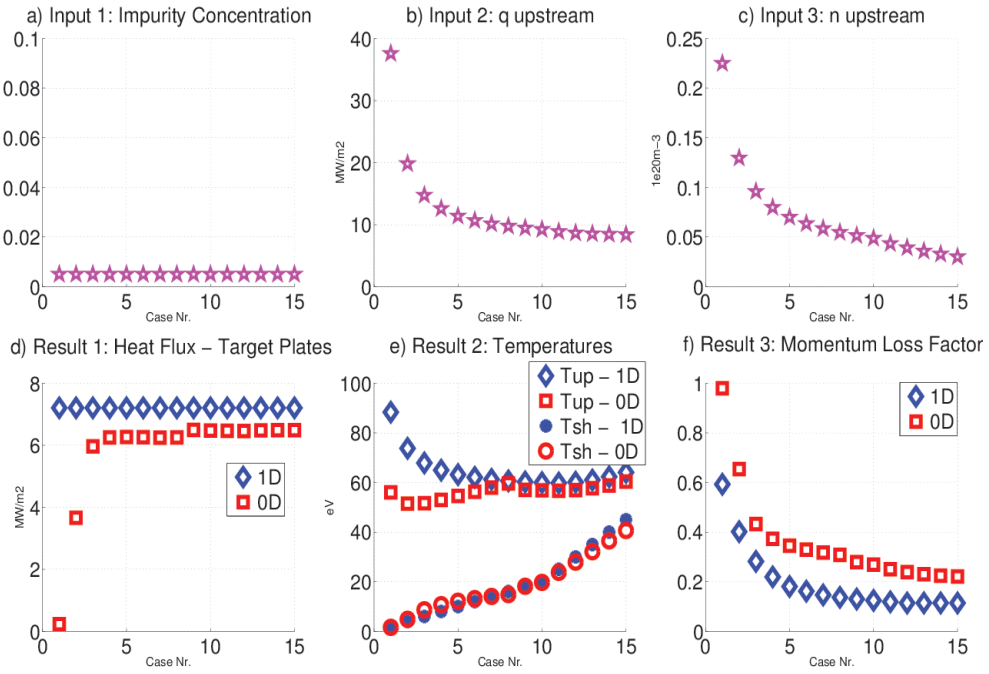


Figure 3: Results of the calibration - low impurity concentration case. The power at the target for the 1D code has been fixed to 0.1 MW, the nitrogen relative concentration amounts to 0.5% and a scan in $T_{sh}$ has been performed. Plots a), b) and c) show the input quantities for the 0D model ($c_z^I = c_z^{II}$, $q_{up}$ and $n_{up}$, respectively), whereas plots c), d) and e) compare the 0D model output quantities ($q_{pl}$, $T_{up}$, $T_{sh}$ and $f_m$) to the corresponding quantities from the 1D calculations. Blue symbols identify 1D results, red symbols 0D results.

and $L_r = L_\parallel$). The upstream power flux $q_{up}$, the upstream particle flux $\Gamma_{up}$ and the impurity concentrations are required in input. For convenience, we

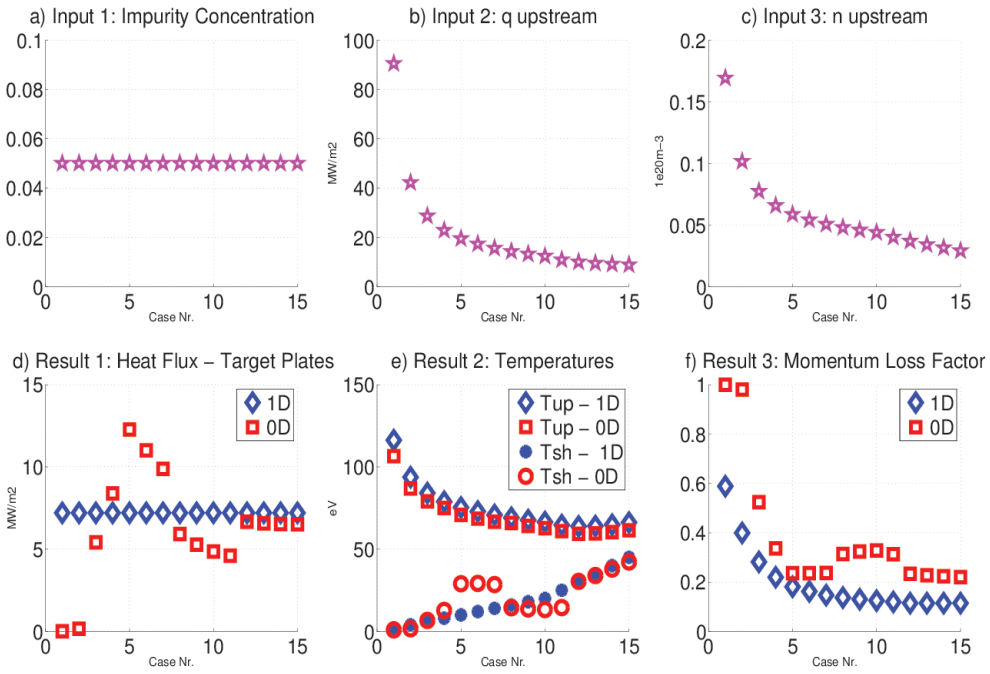


Figure 4: Results of the calibration - high impurity concentration case. The power at the target for the 1D code has been fixed to 0.1 MW, the nitrogen relative concentration amounts to 5% and a scan in $T_{sh}$ has been performed. Plots a), b) and c) show the input quantities for the 0D model ($c_z^I = c_z^{II}$, $q_{up}$ and $n_{up}$, respectively), whereas plots c), d) and e) compare the 0D model output quantities ($q_{pl}$, $T_{up}$, $T_{sh}$ and $f_m$) to the corresponding quantities from the 1D calculations. Blue symbols identify 1D results, red symbols 0D results.

re-write the entire system of equations here:

$$n_{up} = \lambda_p \frac{\Gamma_{up}}{D_r} \tag{20}$$

$$q_{up}^2 = q_I^2 + 2\chi_0 (n_{up} T_{up})^2 c_z^I \int_{T_C}^{T_{up}} \mathrm{d}T \sqrt{T} l_z(T) \tag{21}$$

$$L_r = \chi_0 \int_{T_C}^{T_{up}} \mathrm{d}T \frac{T^{5/2}}{q(T)} \tag{22}$$

$$q_I = \frac{\gamma}{2} e n_{up} T_{up} c_{s0} \sqrt{T_C} \tag{23}$$

$$\int_{T_{sh}}^{T_C} \mathrm{d}T \frac{T^{3/2}}{l_z(T)} = \frac{n_{up} T_{up} c_z^{II}}{\gamma e c_{s0}} L_m \tag{24}$$

$$q_{sh} = \frac{\gamma}{2} e n_{up} T_{up} c_{s0} \sqrt{T_{sh}} \tag{25}$$

$$f_m = 1 - 2\left(\frac{\alpha_{ps}}{1+\alpha_{ps}}\right)^{(\alpha_{ps}+1)/2} \tag{26}$$

$$q_{pl} = (1 - f_m) \frac{\gamma}{2 f_x} e n_{up} T_{up} c_{s0} \sqrt{T_{sh}}, \tag{27}$$

where $q(T)$ in Eq.22 is given by Eq.6. A multi-species generalisation of the model (i.e. considering more than one radiative atomic species at once) is straightforward. Indicating with $c^I_{z,j}$ , $c^{II}_{z,j}$ and $l_{z,j}(T)$ the concentrations and the cooling factor of the $j$-th species, the system Eq.20-27 takes the form

$$n_{up} = \lambda_p \frac{\Gamma_{up}}{D_r} \tag{28}$$

$$q^2_{up} = q^2_I + 2\chi_0 (n_{up} T_{up})^2 \sum_j c^I_{z,j} \int_{T_C}^{T_{up}} \mathrm{d}T \sqrt{T} l_{z,j}(T) \tag{29}$$

$$L_r = \chi_0 \int_{T_C}^{T_{up}} \mathrm{d}T \frac{T^{5/2}}{q(T)} \tag{30}$$

$$q_I = \frac{\gamma}{2} e n_{up} T_{up} c_{s0} \sqrt{T_C} \tag{31}$$

$$\int_{T_{sh}}^{T_C} \mathrm{d}T \frac{T^{3/2}}{\sum_j c^{II}_{z,j} l_{z,j}(T)} = \frac{n_{up} T_{up}}{\gamma e c_{s0}} L_m \tag{32}$$

$$q_{sh} = \frac{\gamma}{2} e n_{up} T_{up} c_{s0} \sqrt{T_{sh}} \tag{33}$$

$$f_m = 1 - 2 \left( \frac{\alpha_{ps}}{1 + \alpha_{ps}} \right)^{(\alpha_{ps}+1)/2} \tag{34}$$

$$q_{pl} = (1 - f_m) \frac{\gamma}{2 f_x} e n_{up} T_{up} c_{s0} \sqrt{T_{sh}}. \tag{35}$$

The free parameters for the calibration are basically two: $T_C$ and $\gamma$. Also, the impurity radiation data can be corrected by means of a numerical factor. The benchmark against a more sophisticated 1D code is discussed in the next section.

# 3 Benchmark

The code against which the benchmark has been performed is the 1D code developed recently by Kallenbach et al [4]. This code solves the continuity, momentum and energy conservation equations for the plasma and a simplified continuity equation for the neutrals along a magnetic field line, thus yielding parallel profiles of densities, velocities and temperatures. As input, it needs power and temperature at the divertor plates - equations are so to say solved "backwards", contrarily to the 0D routine presented here. In order to carry out the benchmark, one has therefore to run a 1D calculation fixing $T_{sh}$ and $P_{Target}$, subsequently employing the calculated $n_{up}$ and $q_{up}$ as input for the 0D routine and then comparing the two results. The impurity radiation data - only one species, nitrogen, has been employed - have been taken from ADAS, assuming a non-coronal parameter $n_e\tau = 0.5$ ms 1e20m$^{-3}$. The connection length of the considered field line has been set to $L_\parallel = 120$ m. Two different scans in $T_{sh}$ (from $T_{sh} = 2$ eV to $T_{sh} = 45$ eV) with $P_{Target}$ fixed at 0.1 MW for different impurity concentrations have been performed. Incidentally, note

that varying $T_{sh}$ for fixed $P_{Target}$ also implies a modification in $n_{up}$ and $q_{up}$, as can be seen in Fig.3 b) and c), as well as in Fig.4 b) and c). The results shown here have been obtained setting $\gamma = 13$ and $T_C = 15$ eV in the 0D routine, the latter value being essentially in agreement with recent experimental observations [17]. The impurity radiation for the conductive region has been corrected with a factor 0.4. The need for such correction is probably due to the fact that, in reality, no "strong" separation between conductive and convective regions exists and therefore, even in a conduction dominated regime, a temperature gradient still survives, weakening the effect of the radiative cooling. Fig.3 shows the results for a nitrogen concentration of 0.5%. As one can see, the agreement on the temperatures is quite good, especially for $T_{sh}$ - which is the most important parameter for the estimate of the detachment degree. The onset of the detachment (i.e. the variation of the slope in the $f_m$ curve) starts to take place at around 3-5 eV (in agreement with [16]), the Self-Ewald model overestimating a bit the value of $f_m$ in comparison to the 1D calculation. A second test has been carried out with a higher impurity concentration - 5% - in order to verify the model under more requiring conditions (as the impurity concentration increases, the difference between a 0D and a 1D routine able to better reproduce the temperature profiles is expected to become more significant). The results are shown in Fig.4. Again, the agreement is quite good, although not as good as before for the reason just elucidated. Nevertheless, the onset of detachment is again quite well reproduced, the errors on $T_{sh}$ being mostly relevant in the non-detached, high $T_{sh}$ cases.

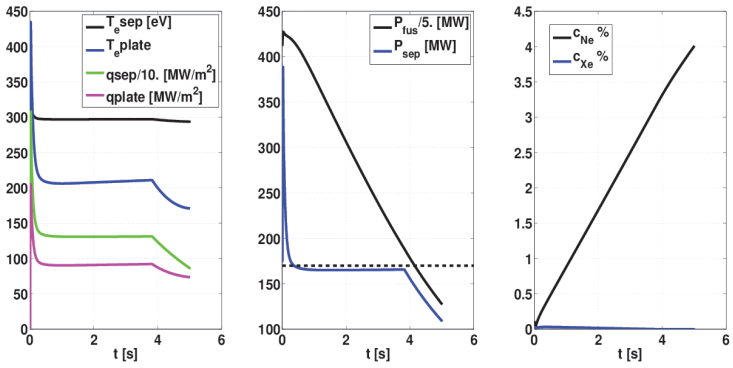


Figure 5: ASTRA Results: Xe-Ne case. The first figure shows the time evolution of the heat fluxes and the temperatures at the outer midplane and on the divertor plate, the second one shows the time evolution of the generated fusion power and of the corresponding $P_{SOL}$, whereas the third one contains the time evolution of the impurity concentrations in the core.

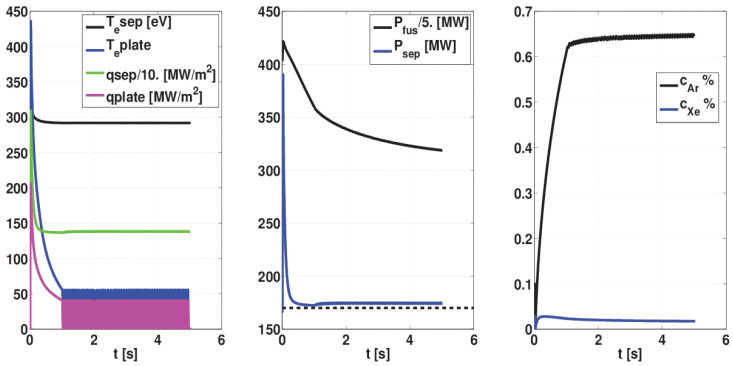


Figure 6: ASTRA Results: Xe-Ar case. The first figure shows the time evolution of the heat fluxes and the temperatures at the outer midplane and on the divertor plate, the second one shows the time evolution of the generated fusion power and of the corresponding $P_{SOL}$, whereas the third one contains the time evolution of the impurity concentrations in the core.

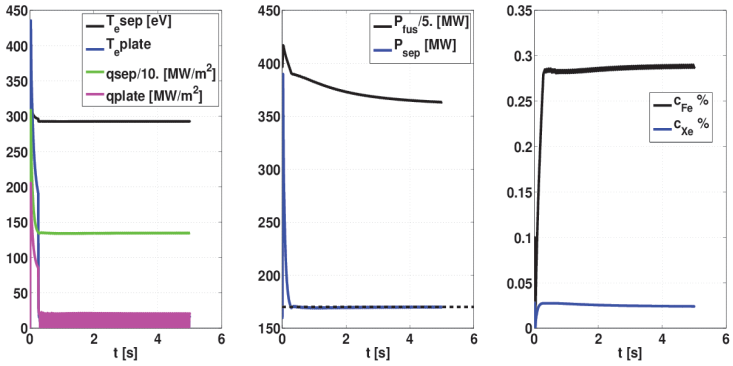


Figure 7: ASTRA Results: Xe-Fe case. The first figure shows the time evolution of the heat fluxes and the temperatures at the outer midplane and on the divertor plate, the second one shows the time evolution of the generated fusion power and of the corresponding $P_{SOL}$, whereas the third one contains the time evolution of the impurity concentrations in the core.

# 4 Applications

In this section, an exemplificative application of the model is presented. The routine has been coupled with the well-known core transport code ASTRA [5, 6] to carry out a preliminary DEMO investigation. ASTRA calculates the density and temperature profiles in the core plasma for a DEMO equilibrium, providing to the 0D routine the required particle flux and the heat flux at the separatrix

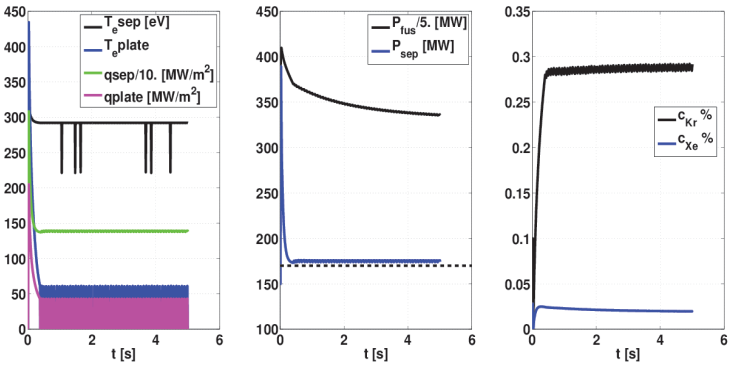


Figure 8: ASTRA Results: Xe-Kr case. The first figure shows the time evolution of the heat fluxes and the temperatures at the outer midplane and on the divertor plate, the second one shows the time evolution of the generated fusion power and of the corresponding $P_{SOL}$, whereas the third one contains the time evolution of the impurity concentrations in the core.

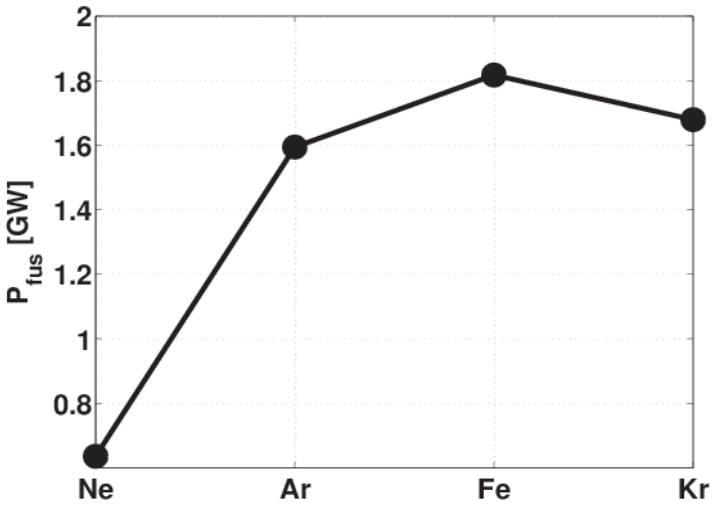


Figure 9: ASTRA Results: Final value of the fusion power as a function of the chosen SOL radiating impurity.

(more correctly, ASTRA calculates the power at the separatrix $P_{SOL}$, which is then converted in the parallel flux $q_{up}$ employing the well known expression

$$q_{up} = \frac{P_{SOL}}{2\pi R \lambda_q \frac{B_{pol}}{B_{tor}}}, \tag{36}$$

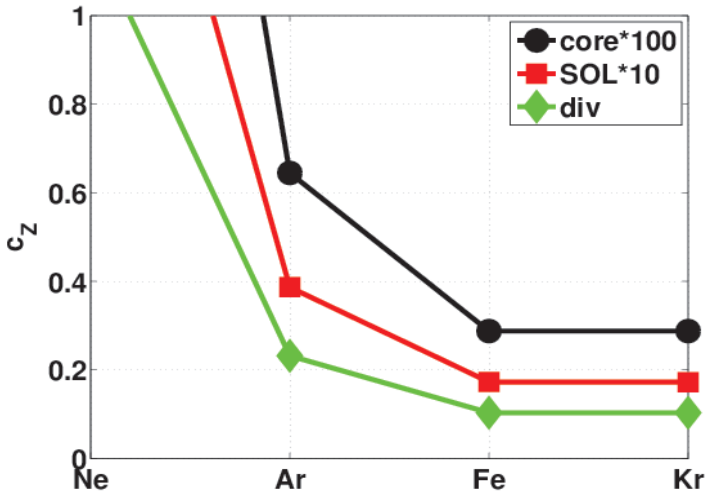


Figure 10: ASTRA Results: Final value of the SOL radiating impurity concentration as a function of the chosen SOL radiating impurity.

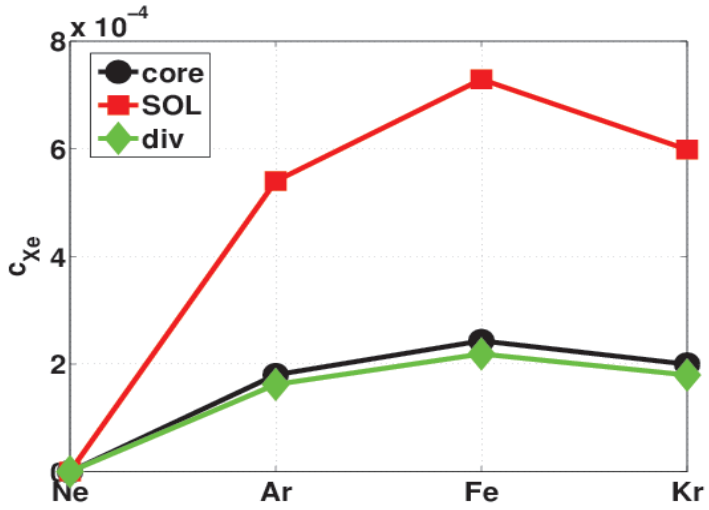


Figure 11: ASTRA Results: Final value of the Xe concentration as a function of the chosen SOL radiating impurity.

where the e-folding length $\lambda_q$ has been set to the value of 1 cm, $R$ is the major radius and $B_{pol}$ and $B_{tor}$ are the poloidal and toroidal component of the magnetic field at the outer midplane, respectively). The multi-species version

of the model (Eq.28-35), with the calibration data determined in the previous section (i.e. $T_C = 15$ eV, $\gamma = 13$ and a non-coronal factor for the conductive region of 0.4) has been employed. The noble gas xenon, which is supposed to play the role of main radiative species for the plasma core (recall that the reactor DEMO is supposed to radiate a fraction of the alpha power of around 75% in the core [7, 9]) is associated to a second atomic species $j$, which is on the contrary employed to radiate in the SOL/Divertor. Xenon is supposed to be puffed at the outer midplane, its concentration in region I, $c^I_{z,XE}$, being therefore connected to its core concentration in a simplified way by means of a constant compression factor $w^{Xe}_{Core,I}$

$$w^{Xe}_{Core,I} \doteq \frac{c^{Core}_{z,Xe}}{c^I_{z,Xe}}, \tag{37}$$

which has been set to the value of 3. Similarly, a compression factor between region I and II,

$$w^{Xe}_{II,I} \doteq \frac{c^{II}_{z,Xe}}{c^I_{z,Xe}}, \tag{38}$$

has been set to the value of 0.3 (this means, in other words, that the Xe concentrations in the core and in the divertor are supposed to be almost equal to one third of the SOL one, where the gas is puffed). The second atomic species $j$ is on the contrary supposed to be puffed directly in the divertor, being therefore more concentrated in region II than in region I or in the core. Specifically, the values

$$w^j_{Core,I} \doteq \frac{c^{Core}_{z,j}}{c^I_{z,j}} = 6 \tag{39}$$

and

$$w^j_{II,I} \doteq \frac{c^{II}_{z,j}}{c^I_{z,j}} = 6 \tag{40}$$

have been set. Clearly, the question whether these compression factors are possible to be achieved in reality with each of the considered $j$-impurities goes beyond the goals of the present analysis. In view of what already mentioned in section one, it is also important to repeat that *when the temperature is everywhere larger than $T_C$, region II is not taken into account in the calculation, and subsequently the value $c^{II}_z$ has no impact at all on the result.* Again, this is due to the fact that the correspondance between region II and divertor volume shall not be understood in a strictly geometrical sense.

Four species $j$ have been considered in the present analysis, namely argon, neon, krypton and iron. ASTRA dynamically calculates the density, temperature and fusion power profiles in the core, providing new values of $q_{up}$ and $n_{up}$ to the 0D model, which in turn determines $q_{pl}$, and dinamically changes the impurity concentrations until the constraints of $P_{SOL} = 170$ MW (i.e. above the predicted value necessary for the L-H transition, see [9]) and $q_{pl} \leq 10$ MW/m$^2$

are fulfilled. In view of the compression factors, it is impossible to change the SOL radiation without affecting the main plasma and viceversa, therefore ASTRA repeats the calculation of the core profiles any time the concentrations are varied. *The goal of this investigation consists in determing which impurity combination is able to fulfill the requirements on $P_{SOL}$ and $q_{pl}$ having at the same time the smallest impact on the performance of the reactor*, which essentially means keeping the fusion power at an acceptable level.

The results of the calculations are shown in Fig.5-11. In Fig.5, one can observe that it has been impossible for ASTRA to find a stationary solution with neon. In fact, a strong deterioration in the fusion power takes places before having achieved a sufficient reduction of the heat flux at the target plate. This because, in spite of the quite high value of $w^j_{Core,I}$, the neon concentration in the main plasma pollutes the core too much in comparison to the little benefits in the SOL. The simulation has been interrupted at $P_{SOL} \simeq 110$ MW, as its continuation would simply have led to a further reduction of the fusion power. On the contrary, a solution has been found for argon, krypton and iron. Observing Fig.6-8, one can notice that the $T_{sh}$ and $q_{pl}$ curves start to violently oscillate after a sufficiently low temperature is reached. This is a consequence of the fact that, when $T_{sh} < T_C$, the conductive region - which has an impurity concentration $c^{II}_{z,j}$ 36 times larger than the core region - comes suddenly into play, dramatically enhancing the radiated power. ASTRA reacts back by correcting the impurity concentration, but this small correction is sufficient to increase $T_{sh}$ above $T_C$ again, this entire sequence leading to the observed oscillating behaviour without however significantly affecting the value of $P_{SOL}$. These sudden jumps in the radiative power could be avoided by means of a non-stationary version of the model, including a more detailed description of the impurity transport, which is however left for future work. Such oscillating regime can be understood as the onset of the detachment, or in other words the final values of the impurity concentrations identify possible DEMO operational points which satisfy the required constraints (the final value of $P_{fus}$ is contained in Fig.9, whereas final concentrations for xenon and for the considered SOL radiative species are shown in Fig.10 and 11, respectively). Interestingly, the best reactor performance has been achieved with iron, which has however the obvious drawback of not being a gas and therefore being impossible to be puffed. Although these calculations are to some extent simplistic, this analysis shows that the performance of a nuclear fusion reactor is crucially connected to the possibility of achieving high impurity concentrations in the SOL without deathly affecting the radiation level in the core.

# 5 Summary and Conclusions

We have developed a 0D, stationary model for the calculation of the divertor detachment onset to be employed in system codes or in general for integrated modelling purposes. The presented model is able to reproduce with a sat-

isfactory accuracy the results of a more detailed 1D code while keeping the calculation times much faster - ∼0.1 sec against ∼1 minute on a single processor. In particular, the temperature at the plates, which represents the key parameter to identify the onset of the detachment, seems to be correctly reproduced. We think that the routine presented here possesses all the necessary features to be employed in the preliminary design of a nuclear fusion reactor like DEMO, as the ASTRA calculations presented in section 4 show. For future work, a more extensive calibration campaign against SOLPS and against experimental data, together with the development of a non-stationary version of the model possibly including a more detailed treatment of impurity transport, are planned.

# 6 Acknowledgment

Useful conversations with Dr. M. Wischmeier are gratefully acknowledged. This work has been carried out within the framework of the EUROfusion Consortium and has received funding from the Euratom research and training programme 2014-2018 under grant agreement No 633053. The views and opinions expressed herein do not necessarily reflect those of the European Commission.

# References

[1] Yu. Igitkhanov *et al.*, 21st EPS, Montpellier, ECA v.18B, 1994

[2] Yu. Igitkhanov *et al.*, 22th EPS, Bournemouth, ECA v.19C, 1995

[3] Yu. Igitkhanov, KIT Scientific Reports 7661 (2014)

[4] A. Kallenbach *et al.*, Plasma Phys. Control. Fusion **58**, 045013 (2016)

[5] G. V. Pereverzev, IPP Report 5/42 (1991)

[6] E. Fable *et al.*, Plasma Phys. Control. Fusion **55**, 124028 (2013)

[7] H. Zohm *et al.*, Nucl. Fusion **53**, 073019 (2013)

[8] R. P. Wenninger *et al.*, Nucl. Fusion **54**, 114003 (2014)

[9] G. Giruzzi *et al.*, Nucl. Fusion **55**, 073002 (2015)

[10] T. Eich *et al.*, Phys. Rev. Lett. **107**, 215001 (2011)

[11] T. Eich *et al.*, Nucl. Fusion **53**, 093031 (2013)

[12] M. Keilhacker. Plasma Physics and Controlled Nuclear Fusion Research, III:183 (1982)

[13] L. L. Lengyel, IPP Report 1/191 (1981)

[14] S. A. Self and H. N. Ewald, Phys. Fluids **9**, 2486 (1966)

[15] C. S. Pitcher and P. C. Stangeby, Plasma Phys. Control. Fusion **39**, 779 (1997)

[16] K. Lackner *et. al*, WPDTT1 - CD02 (unpublished) 2015

[17] A. Leonard *et al.*, Nucl. Fusion **52**, 063015 (2012)